Electronic Supplementary Information (ESI):

MnO_2 nanolayers on highly conductive $TiO_{0.54}N_{0.46}$ nanotubes for supercapacitor electrodes with high power density and cyclic stability

Zhiqiang Wang, *Zhaosheng Li**, *Jianyong Feng*, *Shicheng Yan*, *Wenjun Luo*, *Jianguo Liu*, *Tao Yu*, *and Zhigang Zou**

National Laboratory of Solid State Microstructures, Ecomaterials and Renewable Energy Research Center (ERERC), Department of Physics, Nanjing University, 22 Hankou Road, Nanjing 210093, People's Republic of China.

Experimental and calculation details

The area capacitance (in mF cm^{-2}) of the electrodes from the cyclic voltammetry were calculated according to the following equation:

$$C = \frac{\int Idt}{\Delta E \times S}, \qquad (1)$$

where *I* is the discharge current (in mA) of the discharge process, *ΔE* is the potential window (0.8 V) and *S* is the surface area of the electrode (in cm^2). The integration was conducted over one complete discharge process.

The mass capacitance (in F g^{-1}) of the electrode was calculated from the galvanostatic charge-discharge curve using to the following equation:

$$C = \frac{I \times \Delta t}{\Delta E \times m}, \qquad (2)$$

where *I* is the discharge current (in A) of the discharge process, *Δt* is the time required for the voltage to vary from 0.8 V to 0 V, *ΔE* is the potential window (0.8 V), and *m* is the mass of MnO_2 on the electrode.

For the two electrode system and the devices, the total capacitance (C), energy densities (E) and power densities (P) were calculated by using the following equations:

$$C = \frac{I\Delta t}{\Delta V},$$

$$E = \frac{1}{2}C(\Delta V)^2,$$

$$P = \frac{(\Delta V)^2}{4RM}$$

where I, Δt, ΔV, R, and M are the discharge current density, the discharge time, the voltage window after the deduction of the IR drop in discharge, the internal resistance from IR drop, and the total mass of MnO_2 in both electrodes, respectively.

The internal resistances (R) were determined from the IR drop, *i.e.* voltage drop ΔV_{drop} at the beginning of the galvanostatic discharge curves:

$$R = \frac{\Delta V_{drop}}{2I}$$

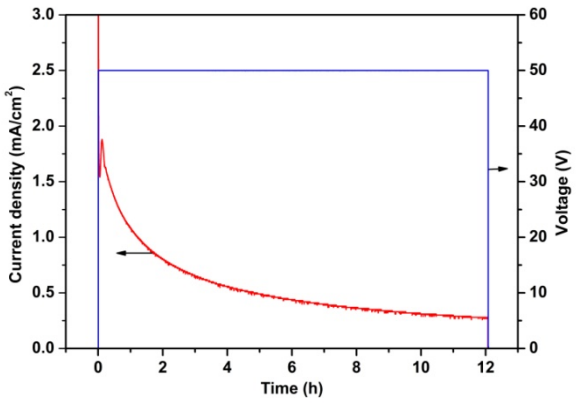

Figure S1. Current and voltage curves of the two electrode system in a classic anodization process.

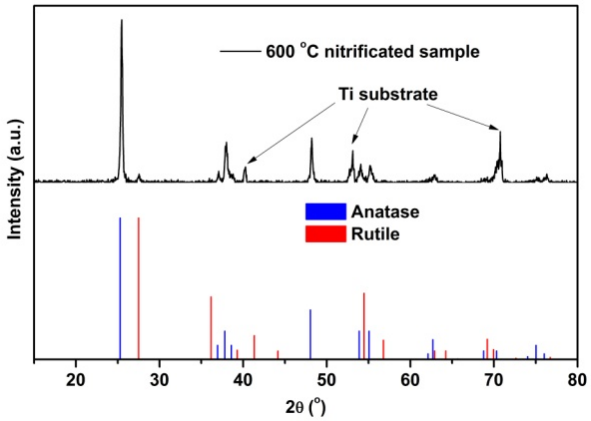

Figure S2. XRD patterns of the titania nanotubes after they were nitrificated at 600 °C.

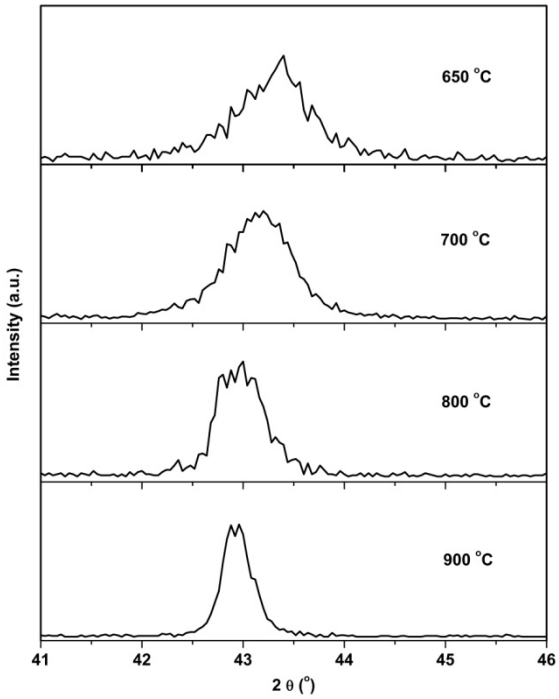

Figure. S3. Dominant XRD peak (200) positions of the $TiO_{1-x}N_x$ nanotubes after they were nitrificated at 650, 700, 800 and 900 °C.

As the nitrification temperature increased, the dominant XRD peak (200) sharpened and the center of the peak shifted to lower 2 theta angles, indicating that the N concentration in $TiO_{1-x}N_x$ increased with the nitrification temperature. XRD patterns confirmed that the amorphous titanate (XRD are not shown here) transformed to cubic TiO_xN_{1-x} when the nitrification temperature was above 650 °C.

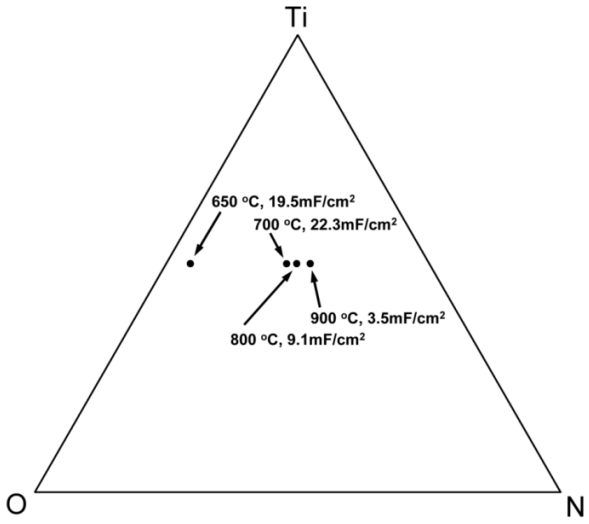

Figure S4. Effect of the nitrification temperature on the component and capacitance of the $TiO_{1-x}N_x$ nanotube arrays.

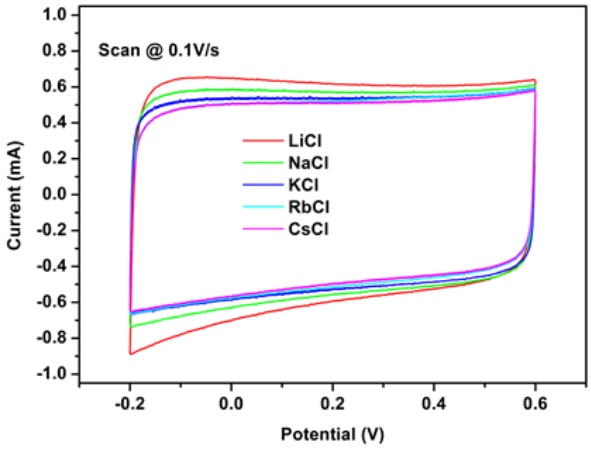

Figure S5. Effect of various aqueous electrolytes (LiCl, NaCl, KCl, RbCl and CsCl) on the performance of $TiO_{1-x}N_x$ nanotube arrays. A three electrode configuration with a scan rate of 0.1 V/s was used. The concentration of the electrolyte was 1.0 mol L^{-1} for all samples.

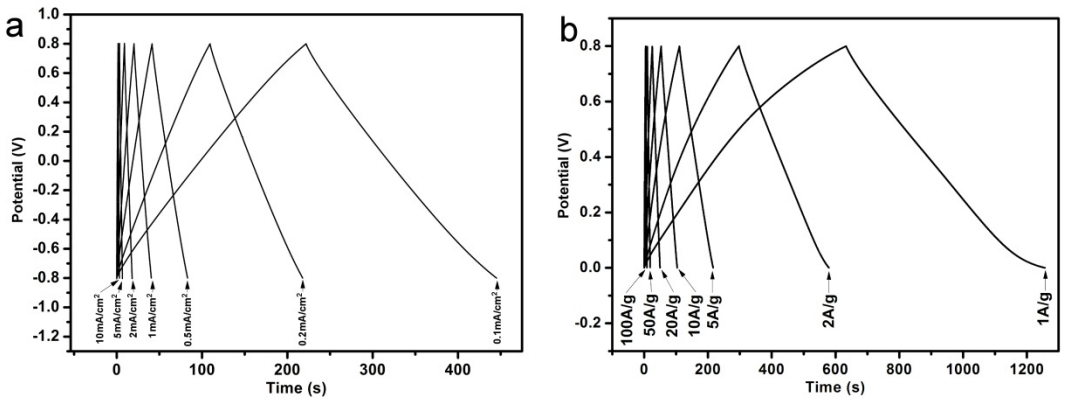

Figure S6. Galvanostatic charge/discharge curves for a three electrode configuration in a 1 mol L^{-1} KCl aqueous solution for (a) $TiO_{0.54}N_{0.46}$ nanotube arrays and (b) MnO_2 on $TiO_{0.54}N_{0.46}$ nanotube arrays (MnO_2 was deposited for 50 s) at various current densities.

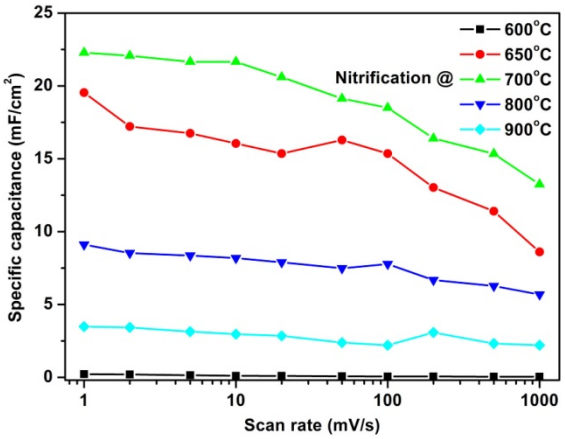

Figure S7. Specific capacitances of TiO_xN_{1-x} nanotube array electrodes calculated using cyclic voltammetray as a function of the scan rate (three electrode configuration, in a 1 mol L^{-1} KCl aqueous solution).

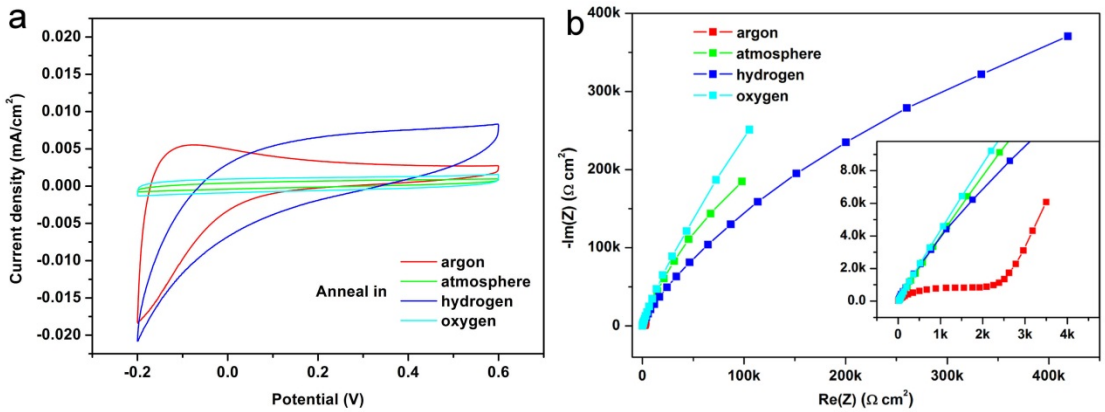

Figure S8. (a) Cyclic voltammetry (0.1 V s^{-1}) of titania nanotube arrays annealed in various gases. (b) Electrochemical impedance spectroscopy (EIS), 0.1 – 10,000 Hz.

For comparison air, oxygen, a hydrogen/nitrogen (1:9) gas mixture and argon were used as the atmosphere in the titania nanotube arrays annealing procedure instead of NH_3 gas. The impedances of these samples were larger than the samples annealed in NH_3 (Fig. 4f). The cyclic voltammetry curves deviated from a rectangular shape for a much lower charge/discharge current and capacitance, compared with those annealed in NH_3.

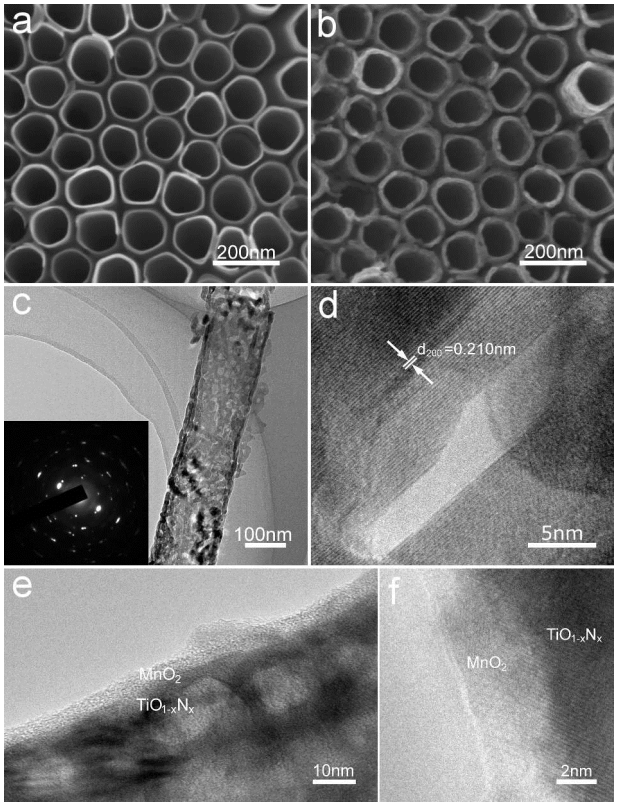

Figure S9. SEM and TEM images of the samples. (a) A titanate nanotube array; (b), (c) and (d) are $TiO_{1-x}N_x$ nanotube arrays nitrificated at 700 °C. (e) and (f) are images of a $MnO_2/TiO_{0.54}N_{0.46}$ interface. The inset in (c) shows the selected area electron diffraction (SEAD) pattern.

Fig. S9a showed that well aligned titanate nanotube arrays with a tube diameter of ~150 nm were formed on flexible titanium foil after anodization and the titanate membranes were connected through regular nanotubes. This enhanced the mechanical strength of the nanotube arrays, inhibiting exfoliation.

Fig. S9b, c and d revealed that $TiO_{0.54}N_{0.46}$ formed nanotube arrays after nitrification at 700 °C. After the nitrification process at temperatures of 650, 700 and 800 °C, the cubic $TiO_{1-x}N_x$ nanotube arrays had similar morphologies to the titanate nanotube arrays, excluding the nanopores on the walls of the nanotubes. Some nanopores in the nanotube walls were observed in the $TiO_{0.54}N_{0.46}$ samples, indicating that $TiO_{0.54}N_{0.46}$ exhibited a hierarchic nanostructure.

Fig. S9c and d showed that many nanopores existed in the walls of the $TiO_{0.54}N_{0.46}$ nanotubes. The inset in Fig. S9c shows the selected area electron

diffraction image of a $TiO_{0.54}N_{0.46}$ nanotube array. This suggested that the $TiO_{0.54}N_{0.46}$ nanotubes were highly crystalline.

Fig. S9e and f showed that MnO_2 was loaded onto the $TiO_{0.54}N_{0.46}$ nanotubes. The surface of the $TiO_{0.54}N_{0.46}$ was covered in MnO_2 with a thickness of 5 – 10 nm for the 100 s deposited samples, which favors improving the conductance.

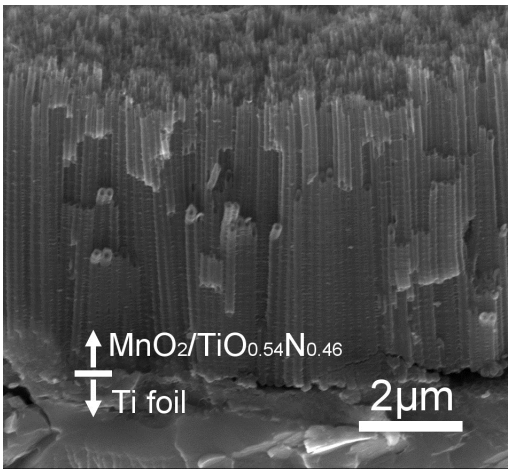

Figure S10. The cross-sectional view of the $MnO_2/TiO_{0.54}N_{0.46}$/Ti.

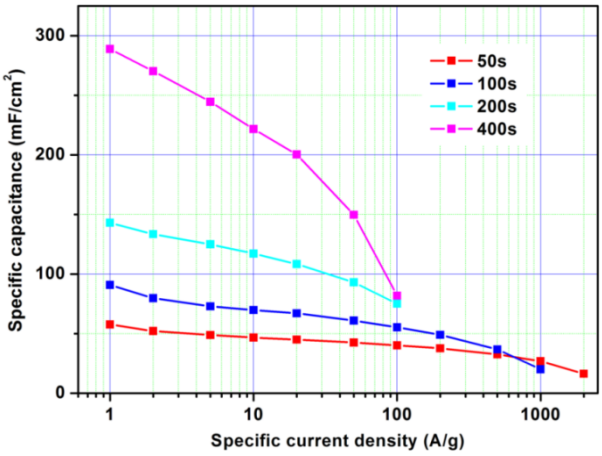

Figure S11. Effect of the MnO_2 loading time on the current density-specific capacitance relationship of MnO_2 on $TiO_{0.54}N_{0.46}$ nanotube arrays (in a three electrode configuration in a 1 mol L^{-1} KCl aqueous solution).

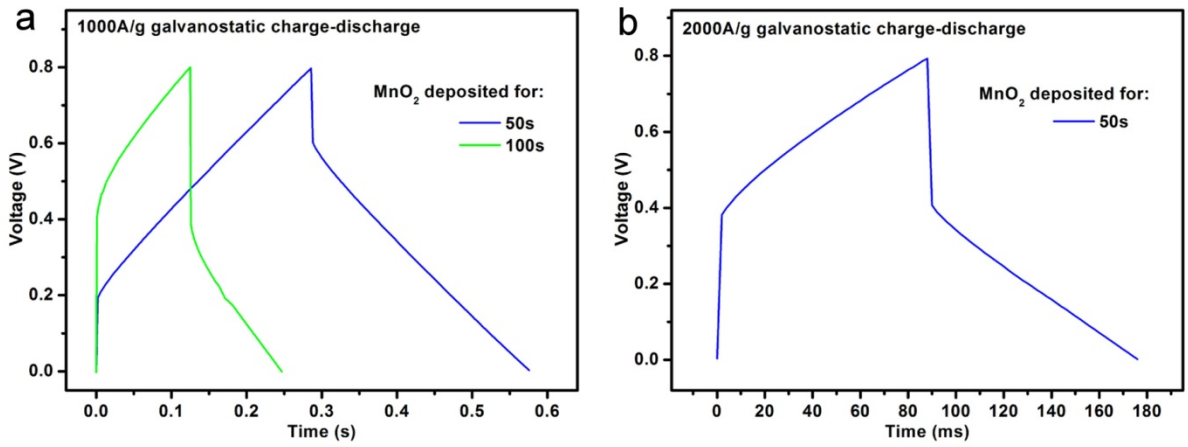

Figure S12. Effect of the MnO_2 loading time on the IR drop for MnO_2 on $TiO_{0.54}N_{0.46}$ nanotube arrays at a current densities of (a) 1000A/g and (b) 2000A/g for a three electrode configuration in a 1 mol L^{-1} KCl aqueous solution.

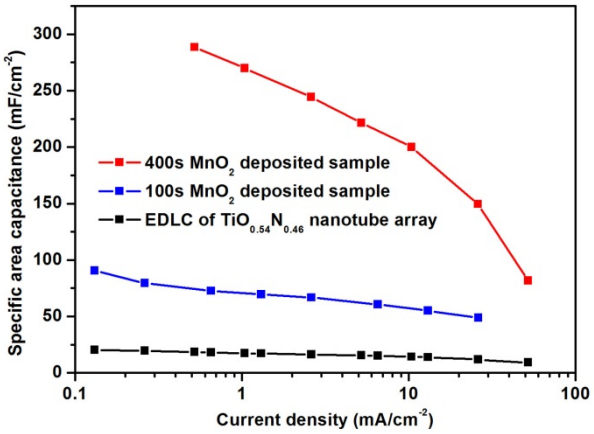

Figure S13. Comparison of the capacitance (in a 1 mol L^{-1} KCl aqueous solution) of $TiO_{0.54}N_{0.46}$ nanotube arrays with the MnO_2-loaded $TiO_{0.54}N_{0.46}$ nanotube arrays for 100 s and 400 s MnO_2 deposited samples at various current densities.

Table S1. Current density in galvanostatic test in Figure S13 (mA cm^{-2})

$TiO_{0.54}N_{0.46}$	**100s MnO_2-deposited $TiO_{0.54}N_{0.46}$**	**400s MnO_2-deposited $TiO_{0.54}N_{0.46}$**
0.131	0.131	
0.262	0.262	
0.521		0.521
0.655	0.655	
1.042		1.042
1.31	1.31	
2.605		2.605
2.62	2.62	
5.21		5.21
6.55	6.55	
10.42		10.42
13.1	13.1	
26.05		26.05
26.2	26.2	
52.1		52.1

In Figure S13, the specific area capacitance of the $TiO_{0.54}N_{0.46}$ nanotubes was measured under the same area current density as the MnO_2-deposited $TiO_{0.54}N_{0.46}$ samples. Note that all of the pseudo capacitive materials had an EDLC portion in their capacitance. The capacitance of the $TiO_{0.54}N_{0.46}$ nanotubes was regarded mainly contributed from the electrochemical double layer capacitance in the mild electrolyte of 1 mol L^{-1} KCl aqueous solution. From Figure S13, it was concluded that the EDLC only took up a very small portion of the total capacitance, and the capacitance of the $MnO_2/TiO_{0.54}N_{0.46}$ electrode mainly comes from the pseudo capacitance of MnO_2.

The mass of the $TiO_{0.54}N_{0.46}$ nanotubes were causiously weighed with a micro balance (METTLER TOLEDO, MX 5) after scratch them from the substrate. The mass of $TiO_{0.54}N_{0.46}$ nanotubes was determined to be 0.12 mg cm^{-2}.

Table S2. Equivalent circuit parameters obtained from the fitting results (corresponding to Fig. 4f). This version of the Warburg element was terminated to be an open circuit.

Loading time of MnO_2	**R1**	**R2**	**C1**	**W1-R**	**W1-T**	**W1-P**
0 s	1.96	0.512	3.76×10^{-5}	1.83	7.19×10^{-3}	0.476
50 s	2.83	0.878	4.89×10^{-5}	1.43	1.36×10^{-2}	0.464
100 s	2.90	1.15	5.52×10^{-5}	1.20	1.80×10^{-2}	0.461
200 s	3.07	1.28	3.99×10^{-5}	1.43	3.37×10^{-2}	0.468
400 s	3.41	1.77	3.17×10^{-5}	2.63	0.116	0.474

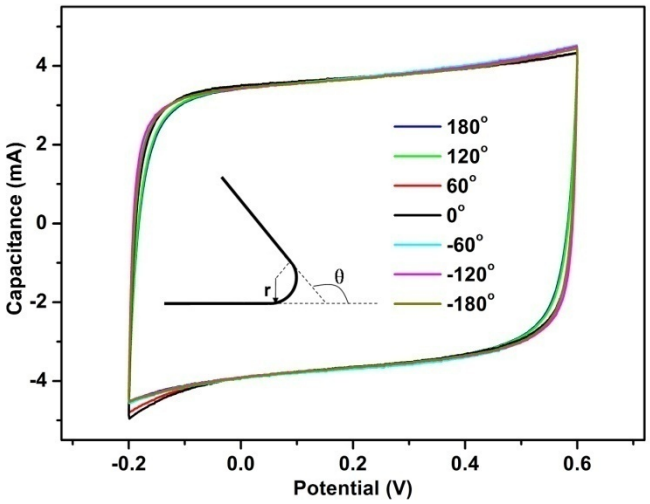

Figure S14. Effect of the folding angle on the capacitance (in a 1 mol L^{-1} KCl aqueous solution) of MnO_2 on $TiO_{0.54}N_{0.46}$ nanotube arrays (r = 5 mm).

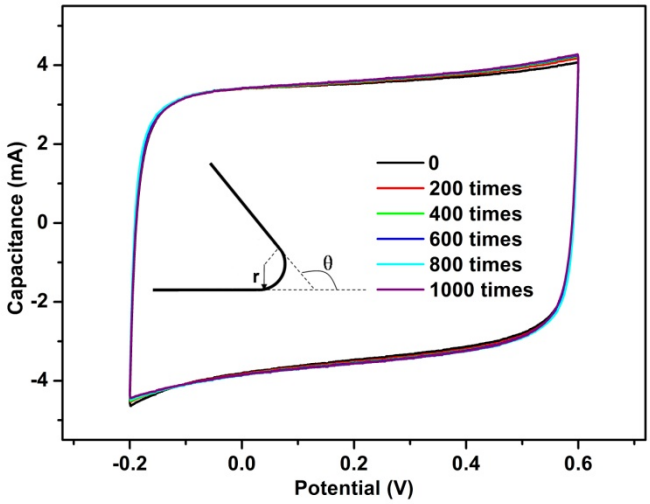

Figure S15. Effect of the folding time on the capacitance (in a 1 mol L^{-1} KCl aqueous solution) of MnO_2 on $TiO_{0.54}N_{0.46}$ nanotube arrays. (r = 5mm, θ ranged from −180 ° to 180 °)

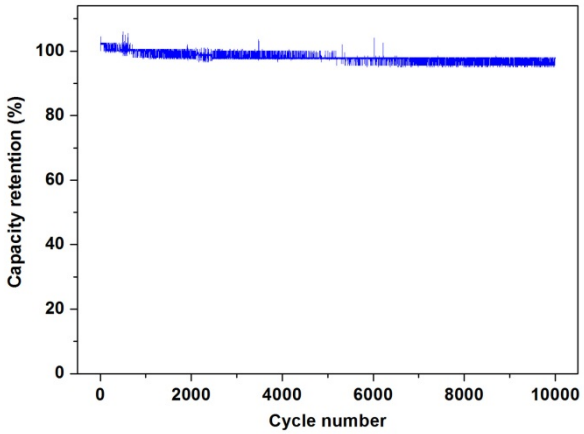

Figure S16. Capacity retention of $MnO_2/TiO_{0.54}N_{0.46}$ supercapacitor devices (with a 1 mol L^{-1} KCl aqueous solution). A capacity retention of 97.5% was recorded after 10,000 galvanostatic cycles.

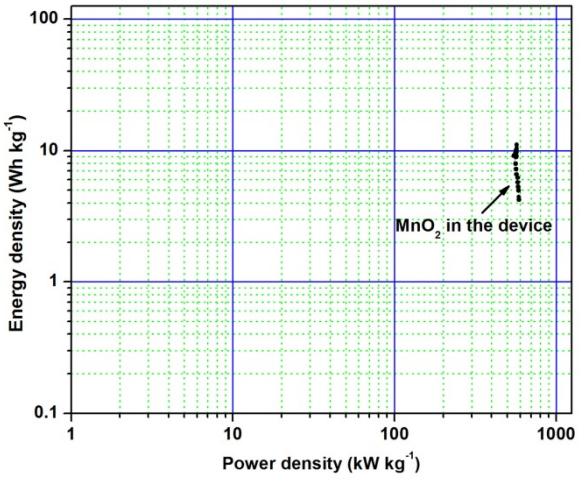

Figure S17. Energy and power densities (Ragone plot) of MnO_2 in $MnO_2/TiO_{0.54}N_{0.46}$ supercapacitor devices.

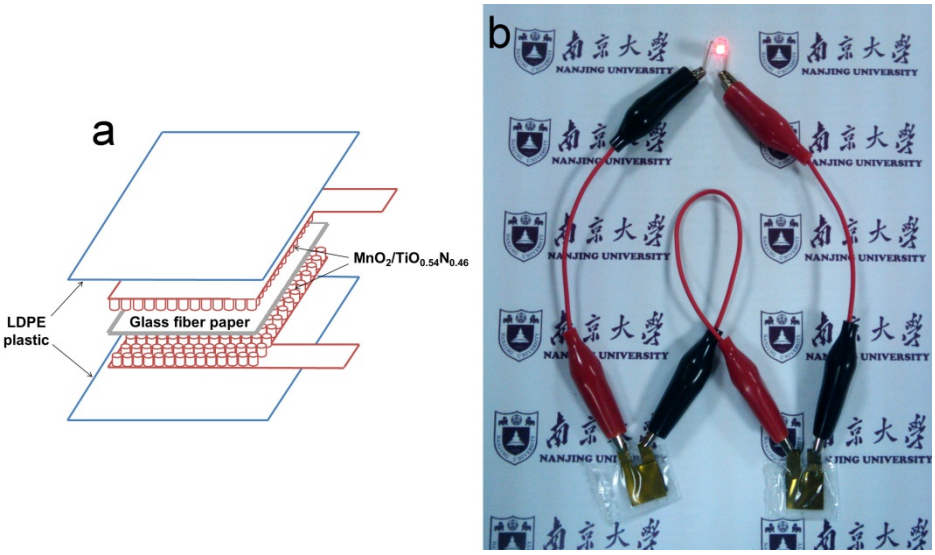

Figure S18. (a) The schematic diagram of the supercapacitor device. (b) A red light emitting diode (LED) powered by two $MnO_2/TiO_{0.54}N_{0.46}$ supercapacitor devices connected in series.

The supercapacitor devices were assembled by two pieces of 100 s deposited $MnO_2/TiO_{0.54}N_{0.46}$ electrodes with a separator (glass fiber paper with pore diameter of 0.26 μm) sandwiched in between, and with 1 mol L^{-1} KCl aqueous solution as electrolyte. Prior to the electrolyte infiltration, the electrodes and the separator were assembled into a rectangular plastic bag (LDPE, low density polyethylene) with sides sealed by 300 °C heated air except the inlet, set aside for the electrolyte injection.

After electrolyte injected and infiltration into the electrode and separator, the inlet was sealed by the 300 °C heated air as before.

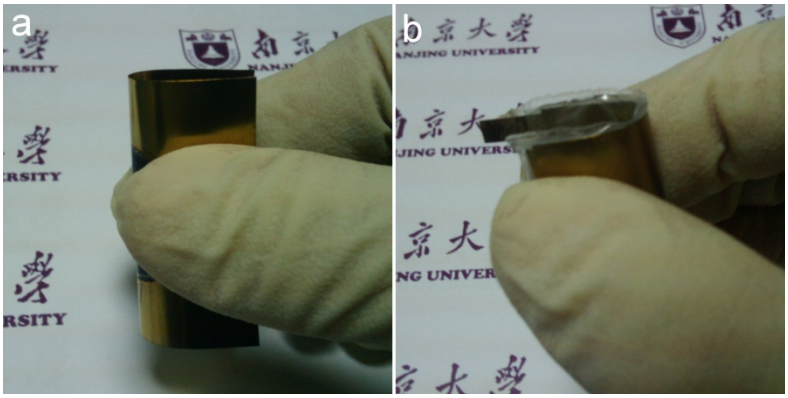

Figure S19. (a) Photo showing the bending of the $MnO_2/TiO_{0.54}N_{0.46}$ electrode in 180 °. (b) Photo showing the bending of the $MnO_2/TiO_{0.54}N_{0.46}$ supercapacitor devices in 180 °.

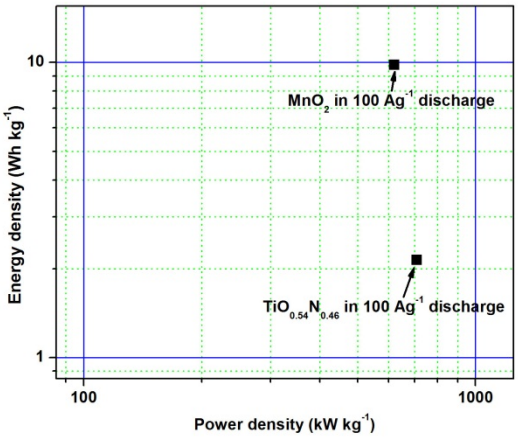

Figure S20. Energy and power densities of MnO_2 compared with that of solely $TiO_{0.54}N_{0.46}$ (Ragone plot, measured in a two-electrode configuration in the discharge current of 100 A g^{-1}).

Table S3. Comparison of the power density and energy density of the MnO_2 and $TiO_{0.54}N_{0.46}$ (*the voltage window, 0-0.8 V; 1 mol L^{-1} KCl aqueous*)

Active materials	**Power density (kW kg^{-1})**	**Energy density (Wh kg^{-1})**
MnO_2 on $TiO_{0.54}N_{0.46}$	620.2	9.8
$TiO_{0.54}N_{0.46}$	708.0	2.1

The energy and power densities of MnO_2 compared with that of solely $TiO_{0.54}N_{0.46}$ nanotubes array have been shown in the Figure S20 and Table S3. Compared to the solely $TiO_{0.54}N_{0.46}$ nanotubes array, the MnO_2 on the $TiO_{0.54}N_{0.46}$ show a relatively higher energy density, because the faradaic reaction of the MnO_2. While due to the low reaction rate of the faradaic reaction, the discharge rate are limited, then the MnO_2 show a relatively lower power density compared to the solely $TiO_{0.54}N_{0.46}$ nanotubes array that accommodate charges in double layer mechanism.